Enhancing extreme ultraviolet photons emission in laser produced plasmas for advanced lithography

T. Sizyuk and A. Hassanein
Center for Materials under Extreme Environment, School of Nuclear Engineering, Purdue University, West Lafayette, Indiana 47907, USA

(Received 3 April 2012; accepted 17 July 2012; published online 1 August 2012)

Current challenges in the development of efficient laser produced plasma sources for the next generation extreme ultraviolet lithography (EUVL) are increasing EUV power and maximizing lifetime and therefore, reducing cost of devices. Mass-limited targets such as small tin droplets are considered among the best choices for cleaner operation of the optical system because of lower mass of atomic debris produced by the laser beam. The small diameter of droplets, however, decreases the conversion efficiency (CE) of EUV photons emission, especially in the case of CO_2 laser, where laser wavelength has high reflectivity from the tin surface. We investigated ways of improving CE in mass-limited targets. We considered in our modeling various possible target phases and lasers configurations: from solid/liquid droplets subjected to laser beam energy with different intensities and laser wavelength to dual-beam lasers, i.e., a pre-pulse followed by a main pulse with adjusted delay time in between. We studied the dependence of vapor expansion rate, which can be produced as a result of droplet heating by pre-pulse laser energy, on target configuration, size, and laser beam parameters. As a consequence, we studied the influence of these conditions and parameters on the CE and debris mass accumulation. For better understanding and more accurate modeling of all physical processes occurred during various phases of laser beam/target interactions, plasma plume formation and evolution, EUV photons emission and collection, we have implemented in our HEIGHTS package state-of-the art models and methods, verified, and benchmarked against laboratory experiments in our CMUXE center as well as various worldwide experimental results. © *2012 American Institute of Physics*. [http://dx.doi.org/10.1063/1.4742159]

I. INTRODUCTION

Currently, significant effort is being devoted to the development of an efficient and debris-free laser produced plasma (LPP) source at 13.5 nm extreme ultraviolet lithography (EUVL).[1,2] Tin is considered to be the target of interest for producing plasmas, as its plasma emits strongly in the EUVL in-band region (13.5 nm with 2% bandwidth), contributed by various ionic stages (Sn^{8+}-Sn^{14+}).[3,4] However, the efficient release of 13.5 nm radiation by the plasma is related to plasma opacity, which depends on level populations of different ionic states, ionization balance, and electron density. The density of the plasma is governed both by laser and target properties. Typically, for nanosecond (ns) LPP, the leading edge of the laser creates plasma, and the remaining part of the laser heats the plasma instead of interacting with the target.

For obtaining the highest conversion efficiency (CE, conversion from laser to EUV in-band radiation) for an EUV LPP source, ideal plasma temperatures and densities should be created for the longest possible period of time with the maximum size. Many previous studies have shown that the EUV emission characteristics of laser-produced Sn plasmas strongly depend on laser and target parameters.[5–8] The main laser parameters that affect the efficiency of EUV light sources include laser wavelength, pulse duration, intensity, spot size, focusing geometry, etc. Currently two laser sources are considered for EUV plasma source production, viz., Nd:YAG (1.06 μm) or CO_2 (10.6 μm). The plasmas produced by both 1.06 μm and 10.6 μm radiate efficiently in the in-band radiation when they possess temperature in the ~30–50 eV range. However, the 10.6 μm laser excitation provides higher conversion efficiency from preheated mass-limited targets[1] or from targets with complex geometry.[6] The major difference between plasmas, created by CO_2 and Nd:YAG lasers, lies in the evolution of their densities, both temporally and spatially.

The process of heating Sn droplets by laser energy results in formation of vapor (detached neutral atoms), fragments (clusters of atoms), and plasma. Final target decomposition to these elements depends on the droplet size and laser beam parameters. Small droplets with sizes of 10–30 μm are considered as perspective targets,[1] since one of the main goals in the development of EUV source for high-volume manufacture is increasing optical components lifetime that is to minimize the debris generation and deposition in the source chamber.

However, small sizes of target leads to utilizing reasonable small spot size of the laser beam and such restriction of sizes results in: (1) increasing the relative part of laser energy for initial heating of the target, since decreasing FWHM of laser beam intensity having Gaussian spatial distribution leads to spending larger part of the energy for heating target surface due to thermal conduction; (2) delaying the processes of vaporization and plasma plume formation, since smaller spot size leads to lower evaporation rate that

results in slower process of vapor/plasma plume formation suitable for laser photons absorption; (3) reducing the size of EUV source area and, therefore, decreasing the brightness of source, and (4) loss of the plasma geometrical confinement, which is related to the hydrodynamic motion of plasma around the spherical target reducing plasma density above the droplet.[5] As a result, small spherical targets give significantly lower CE, especially in the case of CO_2 laser—approximately two times less in comparison with the planar targets heated by the laser with larger spot.

Dual-pulse systems can be used for increasing CE of EUV source from small spherical targets. In this regard, we can consider two modes for utilizing prepared target matter. The first one is based on the heating by the main laser of plasma plume created at the pre-pulse stage and expanded during the short time, up to 100 ns.[8,9] The second one is related to utilizing the evaporated and fragmented parts of the droplet.[1] Heating of this matter is reasonable after delay in the μs range, since velocities of this components is 10–100 times lower than plasma velocity[10] and spatial expansion of such matter to areas covered by the larger plasma spot requires longer time.

Just as a note, previous theoretical[11] and experimental[12] studies showed significant increase of CE due to implementation of dual-pulse with 1064 nm laser as the pre-pulse and 10 μm for the main pulse. However, 1064 nm pre-pulse laser cannot efficiently evaporate the entire droplet due to the relatively low critical density value. For example, low intensity, 5×10^8 W/cm^2, of pre-heating laser in Ref. 11 will lead to the low evaporation rate of 40 μm droplet, considered in this study, that results in large tin debris accumulation in the chamber. High intensities of pre-pulse laser used in Ref. 12 will result in producing tin ions with high energies that also can affect the collecting optics system lifetime.

In this work, we initially modeled the evaporation rate of small droplet in dependence on the pre-pulse laser wavelength. Then, we modeled plasma/vapor expansion developed from the most vaporized target (80% of 30 μm droplet), optimizing delay between pre-pulse and main pulse and then adjusting spot size of the main, CO_2, laser to get efficient conditions for EUV photons output. Experimental results given in Ref. 1 for the same droplet diameter as in our study showed 2.3% CE "with a pre-pulse irradiation" and 3.25% CE "with improved pre-pulse irradiation". We obtained in our simulations 3% CE that is close to the above data. As it is shown in Ref. 12, CE can be higher for larger droplet sizes and can vary from 3.5% to 4%.

Such detailed simulations were possible with our comprehensive and advanced models for the description of plasma physics processes. Our HEIGHTS package contains detailed models for energy deposition, vapor/plasma formation/evolution and magneto hydrodynamic (MHD), thermal conduction in material and in plasma, atomic physics and resulting opacities, detailed photon radiation transport, and interaction between plasma/radiation and target material. These models were described in several publications.[13–15] Below we give a brief description of some of the implemented models.

II. BRIEF MODELS DESCRIPTION

For accurate modeling of various energy inputs from laser radiation, i.e., absorption/reflection in solid/liquid target, absorption/reflection in target vapor, and absorption/reflection in plasma layer, we used experimental optical properties for laser reflection from liquid tin. Laser photons absorption in vapor was simulated based on the main features of the collision-induced absorption such as a quadratic dependence of the absorption coefficient on the density and a weak dependence on the temperature.[16] Inverse bremsstrahlung absorption was used for simulation of laser photons interaction with plasma. The classical value for the absorption coefficient k_{abs}^{las} that describes the collisional absorption mechanism is[17]

$$k_{abs}^{las} = \frac{16\pi Z n_e^2 e^6 \ln\Lambda(\nu)}{3c\nu^2(2\pi m_e k_B T_e)^{3/2}(1-\nu_p^2/\nu^2)^{1/2}}, \quad (1)$$

where e, n_e, m_e, and T_e are the electron charge, density, mass, and temperature, respectively; Ze is the ionic charge; c is the light speed; ν is the frequency of the laser light; $\nu_p = \sqrt{\frac{n_e e^2}{\pi m_e}}$ is the plasma frequency; and k_B is the Boltzmann constant. The Coulomb logarithm is given by[18]

$$\ln\Lambda = \ln\left[\frac{3}{2}\sqrt{\frac{(k_B T_e)^3}{\pi n_e}}\frac{1}{Ze^3}\right]. \quad (2)$$

In our simulations, this Monte Carlo modeling of laser photons absorption and reflection in liquid/vapor/plasma as well as photon transport in plasma interplays with surface vaporization processes. The vaporized layer above the target surface initializes the processes of laser photons absorption in vapor/plasma that prevents their penetration to target surface. At the same time, radiated plasma photons add their energy to further heating of the droplet and this energy load to the target can be significant from the well-developed hot plasma plume.

HEIGHTS package includes detailed model for target vaporization based on target thermophysical properties as well as the kinetics of evaporation. The model establishes the connection between the surface temperature and the net atom flux leaving the surface taking into account the possibility of recondensation.[19] The time-dependent net evaporation rate may be approximated by

$$\begin{aligned} &J(T) = J_e^{eq}, \ \ if\ t < t_v, \\ &J(T) = J_e^{eq}[0.8 + 0.2\exp(-(t-t_v)/10\tau_c)], \ \ if\ t > t_v, \end{aligned} \quad (3)$$

where τ_c is the above-surface vapor collision time; t_v is the preheat time for preparing the vapor zone when recondensation becomes significant; J_e^{eq} is the equilibrium evaporation flux which can be estimated as

$$J_e^{eq}(T) = 5.8 \times 10^{-2}\frac{\alpha\sqrt{A}P_v(T_v)}{\rho(T_v)\sqrt{T_v}}, \quad (4)$$

where α is the sticking probability; A is the atomic mass; $P(T_v)$ is the saturated vapor pressure; $\rho(T_v)$ is the density at the surface; and T_v is the vapor temperature.

The general form of the hydrodynamic equation set for LPP application, taking into account heat conduction and radiation transport, is described in HEIGHTS using two-temperature approximation model given by

$$\begin{aligned}
&\frac{\partial \rho}{\partial t} + \nabla \cdot (\rho \mathbf{v}) = 0, \\
&\frac{\partial \rho \mathbf{v}}{\partial t} + \nabla \cdot (\rho \mathbf{v}\mathbf{v} + p_h) = 0, \\
&\frac{\partial e_h}{\partial t} + \nabla \cdot [\mathbf{v}(e_h + p_h) - \lambda_e \nabla T_e - \lambda_i \nabla T_i - \mathbf{S}_{rad}] = Q_{las}, \\
&\frac{\partial e_i}{\partial t} + \nabla \cdot [\mathbf{v}(e_i + p_i) - \lambda_i \nabla T_i] = Q_{ei}.
\end{aligned} \tag{5}$$

Here, ρ is density of plasma; $\mathbf{v}$ is velocity of plasma; p_h is hydrodynamic pressure; $e_h = e_e + e_i + e_{kin}$ is the total energy; e_e is the electronic component of the plasma energy, which includes thermal energy of electrons and ionization energy; e_i is the ion component of the plasma energy; and $e_{kin} = \frac{\rho v^2}{2}$ is the kinetic energy of the plasma. Analogous to energy, pressure has electron and ion parts: $p_h = p_e + p_i$. The thermal conduction in the plasma is considered as the combined result of the electron $\lambda_e \nabla T_e$ and ion $\lambda_i \nabla T_i$ components, where λ is the conductivity coefficient and T is the temperature. The radiation transport process is represented here as flux $\mathbf{S}_{rad}$ and the laser heating source as Q_{las}. The Q_{ei} term is the energy interchange between electrons and ions.

Since the set of equations has convective terms (hydrodynamic flux) and dissipative terms (heat conduction, laser heating, radiation transport, and electron-ion interaction), we used splitting methods in our numerical algorithm to separate the hyperbolic and parabolic parts.[15,20,21]

Monte Carlo methods are used for modeling the LPP radiation processes: the laser heating, the radiation transport in the plasma, and the EUV output. Monte Carlo methods have the advantage of being relatively straightforward to apply for complex geometries. For radiation transport, radiation fluxes must be determined to solve two main problems: (1) correction of the plasma thermal energy and, as a result, correction of the plasma motion in the device, and (2) determination of the final useful part of the radiation flux (EUV output).

The following expression is used for numerical calculations of the number N of photons emitted in space (from the volume unit in the time interval):

$$N_0 = \int_{E_{\min}}^{E_{\max}} \frac{k_{em}(E,T,\rho)E^2}{\hbar^3 \pi^2 c^2} \left(e^{\frac{E}{T}} - 1\right)^{-1} dE \quad [\mathrm{cm}^{-3}\mathrm{s}^{-1}], \tag{6}$$

where E is the energy of emitted photon [eV]; $E_{\min}, E_{\max}$ are the spectral range [eV]; $k_{em}(E,T,\rho)$ is the emission coefficient [cm^{-1}]; $\hbar = 6.58217 \times 10^{-16}$ [eV·s] is the Planck's constant; $c = 2.9979 \times 10^{10}$ [cm/s] is the speed of light.

Attenuation of light intensity as a result of matter absorption is described by the expression,

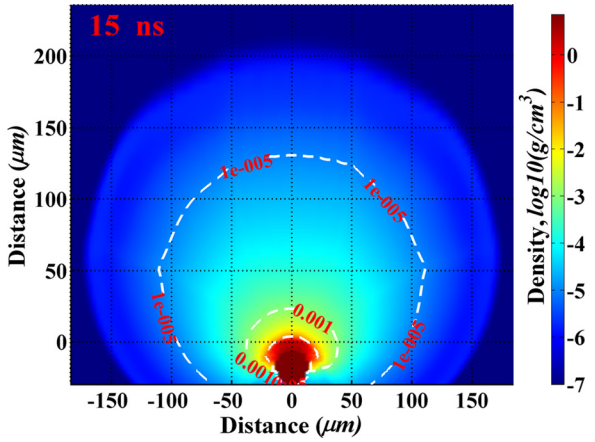

FIG. 1. Mass density distribution at the end of pre-pulse laser beam with 1064 nm wavelength and intensity of 10^{10} W/cm^2.

$$I = I_0 e^{-\int_0^l k_{as}(\omega,l)dl} \tag{7}$$

or, in photon number terms,

$$N(\omega) = N_0(\omega) e^{-\int_0^l k_{abs}(\omega,l)dl}, \tag{8}$$

where $N_0(\omega)$ is the initial number of photons with frequency ω and l is the path length in matter.

To optimize the algorithm and decrease computation costs, we implemented a system of weight factors into the Monte Carlo radiation transport model. Two major weight factors were allocated: normalization of emitted macrophoton relative to most radiated cell of the computational domain and normalization relative to the optical thickness of cell.[22]

We used splitting methods for the solution of Eq. (5) that involve decoupling the full model into separate component for each process, employing specialized numerical methods to solve each component, and coupling the resulting solutions. In case of photon transport, e.g., we simulate photons motion in three-dimensional space, then map resulting energy redistribution onto two-dimensional domain and use it as a correction to plasma thermal energy.

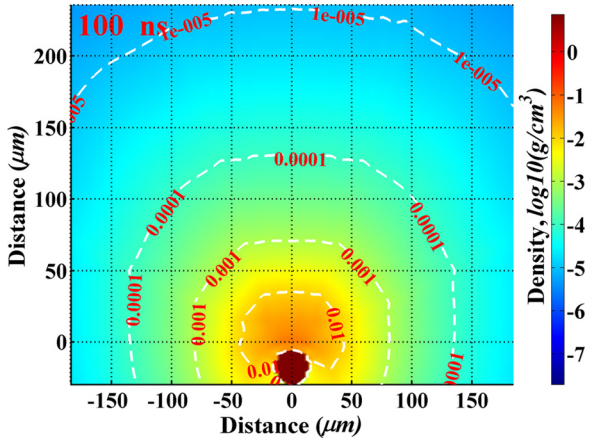

FIG. 2. Mass density distribution after 100 ns delay in pre-plasma created by the laser beam with 1064 nm wavelength and intensity of 10^{10} W/cm^2.

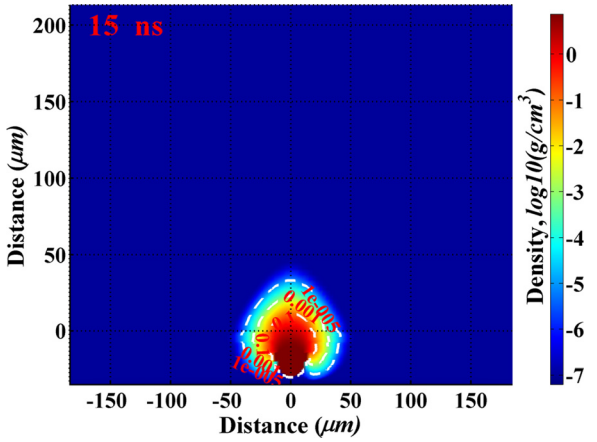

FIG. 3. Mass density distribution at the end of pre-pulse laser beam with 266 nm wavelength and intensity of 10^{10} W/cm^2.

The equations-of-state and opacities are calculated independently for a wide range of temperatures and densities. The structure of atomic energy levels, wavefunctions, transition probabilities, ionization potentials, oscillator strengths, broadening constants, photoionization crosssections and other atomic characteristics are calculated using the self-consistent Hartree-Fock-Slater (HFS) method.[23] The collisional-radiative equilibrium (CRE) model[24] is used to calculate the populations of atomic levels and the ion and electron plasma concentrations. Ion and electron concentrations found from the CRE model are used in the equations of state to calculate the pressure and internal energy.

III. INFLUENCE OF LASER WAVELENGTH AND INTENSITY ON VAPORIZATION DYNAMICS

The mechanisms described above in the formation of laser-produced plasma allow prediction of vaporization rate with acceptable accuracy. For the considered time of the pre-pulse laser duration, 10 ns, we can neglect possible target fragmentation and fragments distribution.

We assumed Gaussian spatial and temporal profiles of laser beam energy and the same beam diameter along laser path in simulated domain. Time counting starts from the beginning of the pre-pulse laser. Figures 1–4 illustrate the

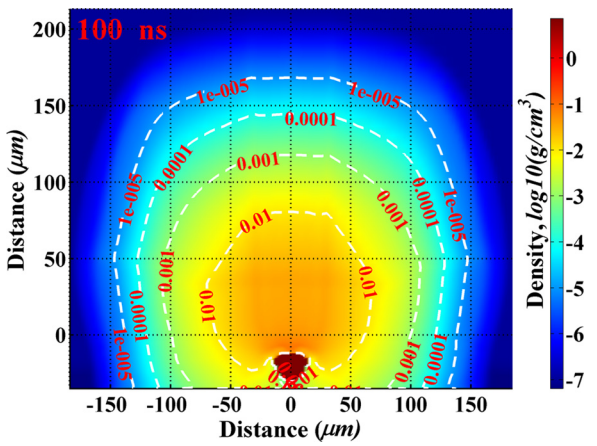

FIG. 4. Mass density distribution after 100 ns delay in pre-plasma created by the laser beam with 266 nm wavelength and intensity of 10^{10} W/cm^2.

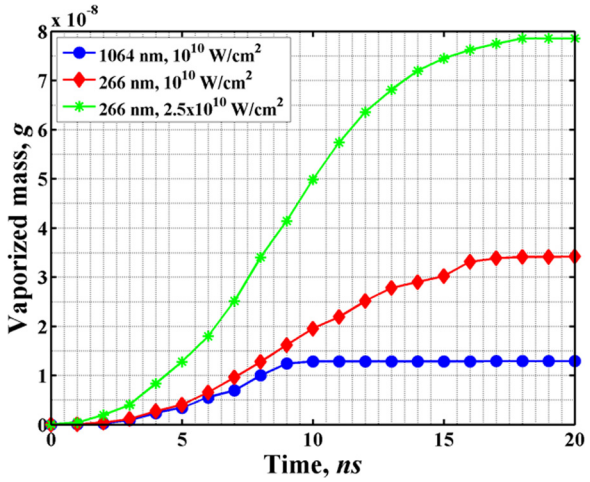

FIG. 5. Dependence of evaporation dynamics on pre-pulse laser wavelength at different intensities. Laser beam parameters used are 30 μm spot size and 10 ns duration.

process of pre-plasma creation, i.e., vaporization and plasma formation by the pre-pulse lasers with two different wavelengths and with the same other parameters such as 10 ns pulse duration and 10^{10} W/cm^2 intensity, 30 μm spot on 30 μm droplet. Tin droplet with this size has mass of 10^{-7} g. Laser beam with 266 nm wavelength and this intensity only vaporized one third of the droplet.

Dependence of vaporization rate on laser parameters has nonlinear tendency since this process, in self-consistent simulation, depends on (1) the time of initiation of laser energy absorption in plasma that reduces energy load to the target; (2) geometry of target, since heating of the droplet by the laser and by the plasma itself can cause vaporization from the sides of droplet. Figure 5 shows evaporated mass during the laser beam pulse for two laser wavelengths. Figure 6 illustrates dependence of droplet vaporization, of the 1064 nm wavelength laser, on the intensity indicating less vaporized mass by more intensive laser beam. Laser with 1064 nm wavelength and high intensity evaporated sufficient mass during the first 2 ns. After this, almost all laser photons were absorbed in the developed plasma plume and the

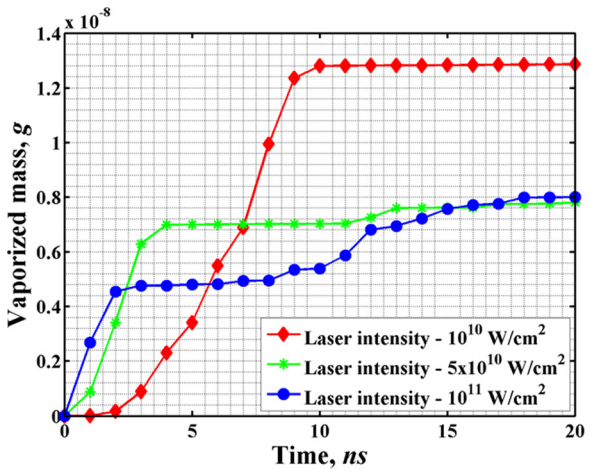

FIG. 6. Dependence of evaporation dynamics on pre-pulse laser intensity at 1064 nm wavelength. Laser beam parameters used are 30 μm spot size and 10 ns duration.

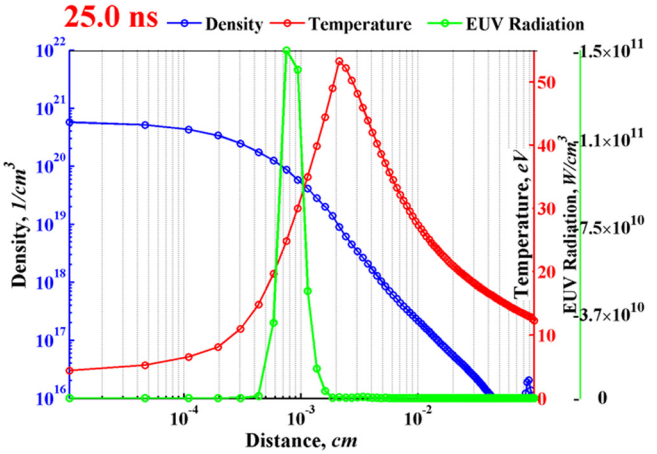

FIG. 7. EUV source location and intensity in relation with density and temperature of plasma created by CO_2 laser.

vaporization rate was low. This case clearly illustrates the vapor shielding effect.[25]

With the same other laser and target parameters, laser with longer wavelength created warmer plasma that was expanded faster (Figs. 1–4), however it vaporized less mass that results in less dense plasma/vapor plume developed during 100 ns.

The advantages of pre-heating small tin droplets by laser with shorter 266 nm wavelength is higher evaporation rate and, therefore, lower accumulation of cluster debris; and lower temperatures of the developed plasma plume therefore lower fluence of energetic ions debris at the pre-pulse stage that can significantly extend optical collecting system lifetime.

IV. PLASMA TEMPERATURE, DENSITY, AND EUV SOURCE LOCATION

The implemented models in HEIGHTS Monte Carlo description for the radiation transport include detailed calculation of opacities that allow precise prediction of EUV source location and strength based on the fundamental description of plasma radiation processes without any adjustments parameters or correlations. These models were benchmarked against CMUXE experimental results[5] as well as

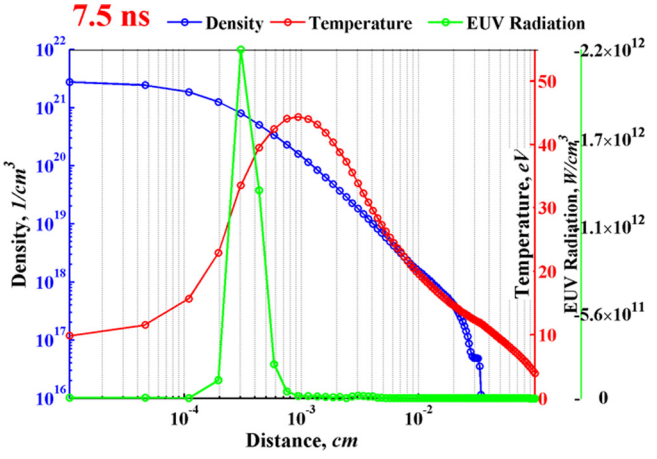

FIG. 8. EUV source location and intensity in relation with density and temperature of plasma created by Nd:YAG laser.

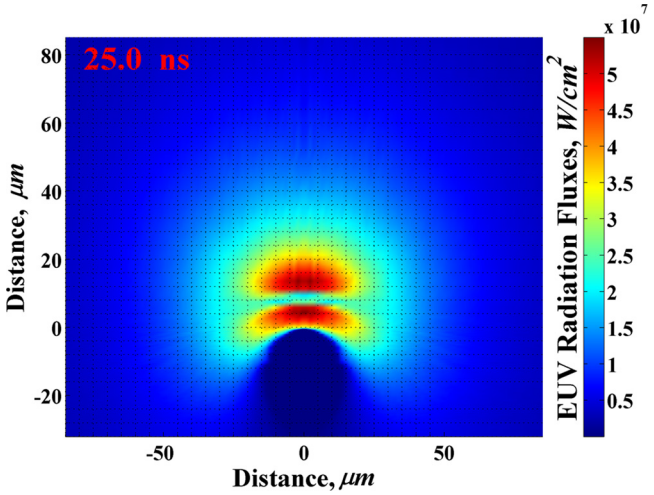

FIG. 9. EUV radiation fluxes in plasma created by CO_2 laser.

with other extensive experimental studies, e.g., by Spitzer *et al.*,[22,26] for various laser beam parameters. We analyzed the dependence of source location and intensity on plasma conditions created by Nd:YAG and CO_2 lasers, and on plasmas heated after the pre-pulse.

Figures 7 and 8 show that optimum temperature for EUV emission is around 30–40 eV in plasmas created by both lasers. Since the 10 μm wavelength is absorbed in region with plasma density of 10^{19} cm^{-3}, location of maximum EUV output is determined by this density value. Laser with 1064 nm wavelength is absorbed by plasma with density 10^{20}–10^{21} cm^{-3} near the target surface that also determines the location of EUV source.

We used in these simulations without pre-pulse the optimized intensities for lasers with considered spot size (30 μm), such as 5×10^{10} W/cm^2 with 30 ns (FWHM) duration for CO_2 and 10^{11} W/cm^2 with 10 ns (FWHM) duration for Nd:YAG. The results shown correspond to the peak intensities of these lasers.

Figures 7 and 8 show also that intensity of EUV source in denser plasma (created by Nd:YAG) is one order of magnitude higher. It is explained by the optical properties of tin

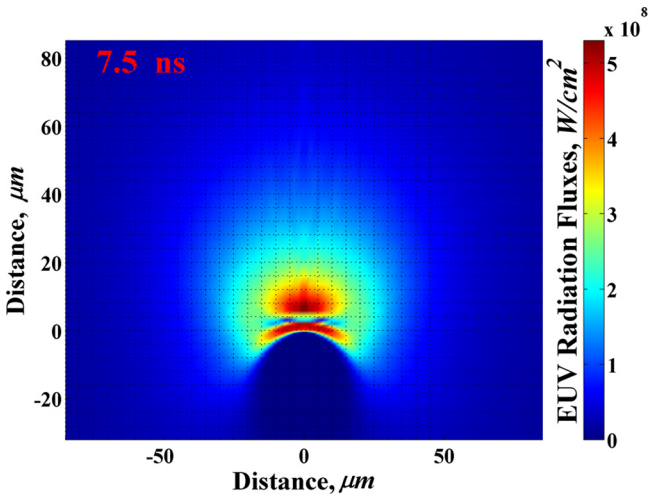

FIG. 10. EUV radiation fluxes in plasma created by Nd:YAG laser.

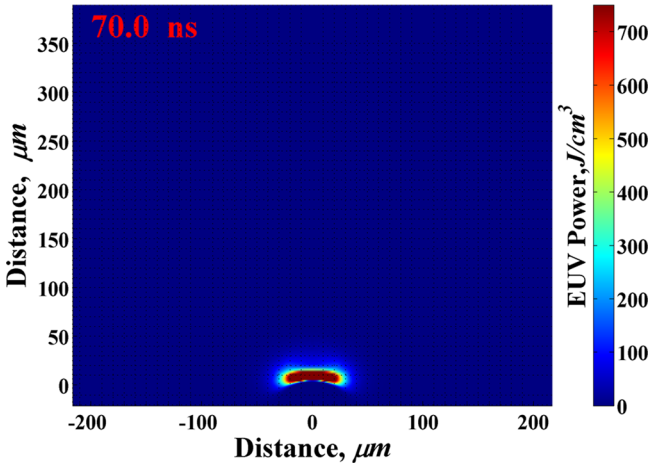

FIG. 11. EUV source collected in 2π sr during 70 ns in plasma created by CO_2 laser without pre-pulse.

plasma with high EUV emissivity at specific temperature values (30–40 eV), where EUV emission (and correspondingly absorption) is increased significantly with density increase, however emission (and absorption also) is decreased suddenly at higher temperature values, located above EUV source. Figures 9 and 10 illustrate EUV energy distribution for the above cases, that is, EUV radiation fluxes (W/cm^2) that describe energy redistribution from the source, i.e., most intensive EUV emission area. EUV source (W/cm^3) in Figs. 7 and 8 corresponds to the area between peaks in figures (for fluxes).

As shown in Figs. 9 and 10, significant part of the emitted photons is absorbed around the source, i.e., in the denser zone closer to the target surface or in the hotter areas above. The EUV radiation fluxes have larger values in surrounding regions. Radiation fluxes in plasma created by Nd:YAG laser are one order of magnitude larger; resulting EUV radiation power, reached the walls of the modeled chamber or the collecting location, is several times higher.

In these cases modeling was done for 30 μm Tin droplet. We obtained 1.3% CE for Nd:YAG laser and 0.45% for CO_2. The high reflectivity of the 10 μm laser and the small spot size are reasons of the low EUV intensity source and the

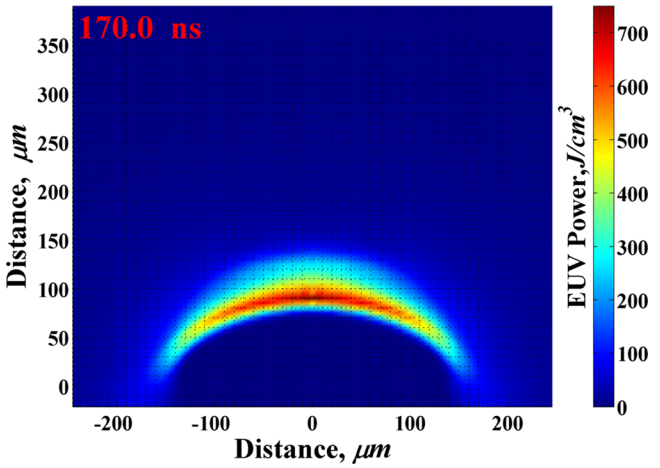

FIG. 12. EUV source collected in 2π sr during 70 ns in plasma created by CO_2 laser with pre-pulse.

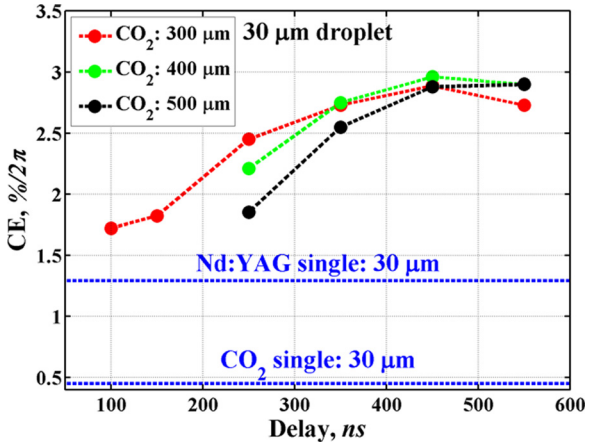

FIG. 13. CE from 30 μm droplet as function of delay between pulses and spot size of CO_2 laser.

small volume of EUV emitting area, created by this wavelength that also results in very low efficiency. Pre-plasma created by shorter wavelength extends the area suitable for CO_2 wavelength absorption. Figures 11 and 12 show location and intensity of EUV power collected in 2π sr during 70 ns from the plasma created by CO_2 laser without (Fig. 11) and with pre-pulse (Fig. 12). In the second case, pre-plasma was created by 266 nm wavelength and expanded during 100 ns before the main pulse with 300 μm spot size impacted. For this case we obtained 1.7% CE.

V. MODELING RESULTS FOR PERFECTLY VAPORIZED TARGET

Laser beam with 266 nm wavelength and intensity of 2.5 $\times$ 10^{10} W/cm^2 vaporized 80% of 30 μm droplet (Fig. 5). To evaluate the efficiency of the prepared plasma/vapor plume for EUV photons output, we used the same CO_2 laser intensity, 7.5 $\times$ 10^9 W/cm^2, and pulse duration, 30 ns. We varied delay time and spot size of the main laser. Figure 13 shows results of optimization of these two parameters. The CE from 30 μm droplet with CO_2 and Nd:YAG laser without pre-pulse are given for comparison.

VI. CONCLUSION

Optimization of EUV sources from small droplet targets using dual laser pulses depends on many parameters and requires detailed analyses of pre-plasma conditions. HEIGHTS comprehensive simulation package, used in this analysis, includes detail models for energy deposition, vapor/plasma formation/evolution and MHD, thermal conduction in material and in plasma, atomic physics and resulting opacities, detailed photon radiation transport, and interaction between plasma/radiation and target material. For 1064 nm pre-pulse laser, tin evaporation rate decreased with increasing laser beam intensity from 10^{10} to 10^{11} W/cm^2, utilizing the same spot size as droplet diameter. Laser with 266 nm wavelength, penetrating deeper to the target, created denser but colder plasma/vapor plume that required more time for expansion to be efficient for the absorption of the 10 μm wavelength. Overall, efficient EUV source depends on combination of

various parameters including pre-pulse laser wavelength/intensity, initial size of target/vaporization rate, and delay time/spot size. We showed ways of maximizing EUV emission based on vaporization processes and adjustments of delay time and main spot size for specific created pre-plasma. We did not indicate that we have received the highest possible CE. Further detail study is required for the maximization of EUV photon emission.

ACKNOWLEDGMENTS

This work is partially supported by the College of Engineering, Purdue University. We gratefully acknowledge the computing resources provided by the Fusion cluster operated by the Laboratory Computing Resource Center at Argonne National Laboratory.

[1]H. Mizoguchi, T. Abe, Y. Watanabe, T. Ishihara, T. Ohta, T. Hori, T. Yanagida, H. Nagano, T. Yabu, S. Nagai, G. Soumagne, A. Kurosu, K. M. Nowak, T. Suganuma, M. Moriya, K. Kakizaki, A. Sumitani, H. Kameda, H. Nakarai, and J. Fujimoto, Proc. SPIE **7969**, 7969–08 (2011).
[2]D. Campos, S. S. Harilal, and A. Hassanein, J. Appl. Phys. **108**, 113305 (2010).
[3]V. Morozov, V. Tolkach, and A. Hassanein, Argonne National Laboratory Report No. ANL-ET-04/24, 2004.
[4]H. Tanuma, H. Ohashi, S. Fujioka, H. Nishimura, A. Sasaki, and K. Nishihara, J. Phys.: Conf. Ser. **58**, 231–234 (2007).
[5]A. Hassanein, V. Sizyuk, T. Sizyuk, and S. Harilal, J. Micro/Nanolith. MEMS MOEMS **8**(4), 041503 (2009).
[6]S. S. Harilal, T. Sizyuk, V. Sizyuk, and A. Hassanein, Appl. Phys. Lett. **96**, 111503 (2010).
[7]Y. Tao, M. S. Tillack, K. L. Sequoia, R. A. Burdt, S. Yuspeh, and F. Najmabadi, Appl. Phys. Lett. **92**, 251501 (2008).
[8]A. Hassanein, T. Sizyuk, V. Sizyuk, and S.S. Harilal, J. Micro/Nanolith MEMS MOEMS **10**, 033002 (2011).
[9]M. S. Tillack and Y. Tao, in Proceedings of 2011 International Workshop on EUV Lithography, Maui, HI, June 2011.
[10]A. Endo, in Proceedings of 2011 International Workshop on EUV and Soft X-Ray Sources, Ireland, 7–10 November 2011.
[11]K. Nishihara, A. Sunahara, A. Sasaki, M. Nunami, H. Tanuma, S. Fujioka, Y. Shimada, K. Fujima, H. Furukawa, T. Kato, F. Koike, R. More, M. Murakami, T. Nishikawa, V. Zhakhovskii, K. Gamata, A. Takata, H. Ueda, H. Nishimura, Y. Izawa, N. Miyanaga, and K. Mima, Phys. Plasmas **15**, 056708 (2008).
[12]S. Fujioka, M. Shimomura, Y. Shimada, S. Maeda, H. Sakaguchi, Y. Nakai, T. Aota, H. Nishimura, N. Ozaki, A. Sunahara, K. Nishihara, N. Miyanaga, Y. Izawa, and K. Mima, Appl. Phys. Lett. **92**, 241502 (2008).
[13]V. Sizyuk, A. Hassanein, and T. Sizyuk, J. Appl. Phys. **100**, 103106 (2006).
[14]V. Sizyuk, A. Hassanein, and V. Bakshi, J. Micro/Nanolith. MEMS MOEMS **6**, 043003 (2007).
[15]V. Sizyuk, A. Hassanein, V. Morozov, V. Tolkach, T. Sizyuk, and B. Rice, Numer. Heat Transfer, Part A **49**, 215–236 (2006).
[16]G. G. Grigoryan, A. G. Leonov, E. A. Manykin, A. A. Rudenko, M. G. Sitnikov, and A. N. Starostin, J. Exp. Theor. Phys. **97**, 678–687 (2003).
[17]T. W. Johnston and J. M. Dawson, Phys. Fluids **16**, 722 (1973).
[18]L. Spitzer, *Physics of Fully Ionized Gases*, 2nd ed. (Interscience, New York, 1962).
[19]A. Hassanein, G. L. Kulcinski, and W. G. Wolfer, Nucl. Eng. Des. Fusion **1**, 307–324 (1984).
[20]G. V. Miloshevsky, V. A. Sizyuk, M. B. Partenskii, A. Hassanein, and P. C. Jordan, J. Comp. Phys. **212**, 25 (2006).
[21]V. M. Kovenya, S. G. Cherny, and A. S. Lebedev, in *Computational Fluid Dynamics*, edited by G.S. Davis and C. Fletcher (North-Holland, Amsterdam, 1988).
[22]V. Sizyuk, A. Hassanein, and T. Sizyuk, Laser Part. Beams **25**, 143–154 (2007).
[23]F. Herman and S. Skillman, *Atomic Structure Calculations* (Prentice Hall, Englewood Cliffs, 1963).
[24]D. Zaltzmann, *Atomic Physics in Hot Plasmas* (Oxford University Press, New York, 1998), Chap. 4.
[25]A. Hassanein, Fusion Eng. Des. **60**, 527–546 (2002).
[26]R. C. Spitzer, T. J. Orzechowski, D. W. Phillion, R. L. Kauffman, and C. Cerjan, J. Appl. Phys. **79**, 2251 (1996).